Emulsions that Store Oxygen for Fast ORR Kinetics and Multifunctional Robotic and Mobility Systems.

*Alissa C. Johnson[1], Alice S. Fontaine[1], Emily A. Beeman[2], James H. Pikul[1,3]**

[1]Department of Mechanical Engineering and Applied Mechanics, University of Pennsylvania Philadelphia, PA 19104, United States of America

[2]Department of Materials Science and Engineering, University of Pennsylvania Philadelphia, PA 19104, United States of America

[3]Department of Mechanical Engineering, University of Wisconsin-Madison, Madison, WI, 53705, United States of America

KEYWORDS

Multifunctional Energy Storage, Catholyte, Air Cathode, Flow Battery, Zinc Air Battery, Soft Actuators

ABSTRACT

Many processes such as catalysis, energy transport, and carbon capture rely on the transport or storage of gases in liquid phases, but the low solubility of gases in liquids limit the rate and efficiency of these processes. Human circulatory systems store large concentrations of oxygen and provide it continuously and simultaneously to trillions of cells without the need for each cell to access the surrounding environment. Inspired by biological circulatory systems, we envision future robotic systems with multifunctional, fully integrated, air-rechargeable energy delivery and storage. This paper presents a high-pH aqueous air catholyte emulsion (ACE) with high oxygen solubility so that metal-air batteries can derive energy entirely from dissolved oxygen. With only 20% silicone oil by volume, ACEs can store twice as much dissolved oxygen (15 mg/L) as pure KOH samples, remain stable for several months, and show superior oxygen reduction reaction kinetics compared to KOH. Zinc-air flow cells with fully submerged electrodes can achieve 4.6 mW/cm2 at 5.6 mA/cm^2. A multifunctional actuator flow cell configuration employs an ACE as both a hydraulic actuator and energy storage fluid, demonstrating the feasibility of ACEs as multifunctional, flexible power sources for soft robotic systems.

1. Introduction

Catalysis, cellular respiration, energy transport, carbon capture, and industrial chemical production are all processes that rely on the transport or storage of gases in liquid phases. The low solubility of gasses, however, limit the rate and efficiency of these processes[1–5]. Porous liquids that increase the oxygen solubility in water by storing the gas in metal-organic materials are overcoming the limitations of traditional chemical processes and have been shown to enhance oxygen reduction reaction (ORR) catalysis and electrolysis in neutral or acidic environments[1,2]. The metal-organic frameworks that enable the high solubility in porous liquids, however, are not compatible with alkaline electrolytes, such as those used in metal-air batteries and fuel cells. Although a nascent technology, there is strong motivation to develop new forms of porous liquids that expand their current stability limitations and provide access to a wider variety of electrolytes.

Metal-air batteries have high theoretical energy densities because their cathode active material is oxygen which can be stored off-board and readily replenished from the environment[6]. Managing oxygen mass transport at the triple-phase boundary between gaseous oxygen, liquid electrolyte, and solid catalyst particles remains a critical challenge[7–11]. Air electrodes, and, on a larger scale, air battery stacks, require airflow channels such that sufficient oxygen can access reaction sites at the triple-phase boundary[12,13]. These semi-open systems are then prone to electrolyte leakage, evaporation, and contamination[13–17]. Some air batteries have demonstrated the ability to extract energy solely from dissolved oxygen; however, the low oxygen solubility and diffusivity in aqueous electrolytes can be performance limiting[18,19]. We hypothesize that a high-pH aqueous fluid with high oxygen solubility can enable sufficiently fast ORR kinetics so that metal-air batteries, and other fuel cells systems, can forgo the complex air-water-catalyst interface and the challenges that come with it.

In addition, liquids with high gas solubility can provide new ways to deliver chemicals and power to distributed systems. The vascular systems in animals provide an excellent example (Figure 1A). The vascular system's ability to transport oxygen to each cell takes advantage of the high energy density of oxygen reduction processes without the need for each cell to access the surrounding environment. This critical feature enables the morphogenic shape of multicellular organisms and animals. Volumetrically, human blood can dissolve 30 times as much oxygen as pure water at 21°C. This high concentration, enabled by hemoglobin's ability to chemically bind oxygen, is critical to achieve the necessary energy flux to sustain life.

In addition to transporting oxygen, energy systems in biology are multifunctional[20]. Fat tissue is the main source of energy storage for the body, but fat also provides insulation, protects organs, serves as a nutrient reserve, and helps to regulate hormones. Animal circulatory systems use blood to transport oxygen and nutrients while simultaneously regulating temperature, removing waste, and helping to fight infection. Inspired by biology, recent work has shown how multifunctional fluids can increase the total energy density of a robotic fish by both storing electrochemical energy and transmitting mechanical work to hydraulic actuators[21]. Despite the moderate energy density of the zinc-iodide electrolytes, this multifunctional approach increased the robot energy density by 4X compared to the same robot powered by just a lithium-ion battery[21].

Combining multifunctional fluidic energy storage with the high energy density of air-replenishable oxygen reduction chemistry will unlock the potential for higher energy density soft robotic systems (Figure 1B). Creating an electrolyte with high oxygen solubility is a fundamental first step toward achieving an air-rechargeable, multifunctional flow battery. Silicone oils are known to have high oxygen solubility (~60X higher than water) and diffusivity (~30X higher than

water), and have been used to improve oxygen transport in air electrodes, increase oxygen transfer rates in aerobic bioreactors, as well as part of synthetic blood to help support the respiration needs of small mammals[22–30]. Silicone oils have also exhibited the ability to form stable emulsions when dispersed in an aqueous phase[31–35]. Thus, silicone oils are promising suspensions for porous liquids which store dissolved oxygen (Figure 1C).

This work demonstrates an air catholyte emulsion (ACE) capable of storing 15 mg/L of dissolved oxygen and delivering air to high-energy zinc air flow batteries with fully submerged electrodes. Our catholyte is an emulsion with silicone oil droplets suspended in 0.5M potassium hydroxide, stabilized by a surfactant (Span-60). A fully submerged cathode can extract energy directly from the oxygen in this fluid without the need to be exposed to surrounding air or maintain a triple-phase boundary in a gas diffusion electrode. An ACE can remain stable for several months, shows superior ORR kinetics compared to 0.5 M KOH, and can be re-oxygenated with atmospheric air. We can achieve 4.6 mW/cm^2 peak instantaneous power density at 5.6 mA/cm^2 discharge current density in a stationary tubular flow cell (STFC) configuration. A multifunctional actuator flow cell (MAFC) demonstrates the ability for emulsion catholytes to enable multifunctional, flexible power sources for soft robotic systems.

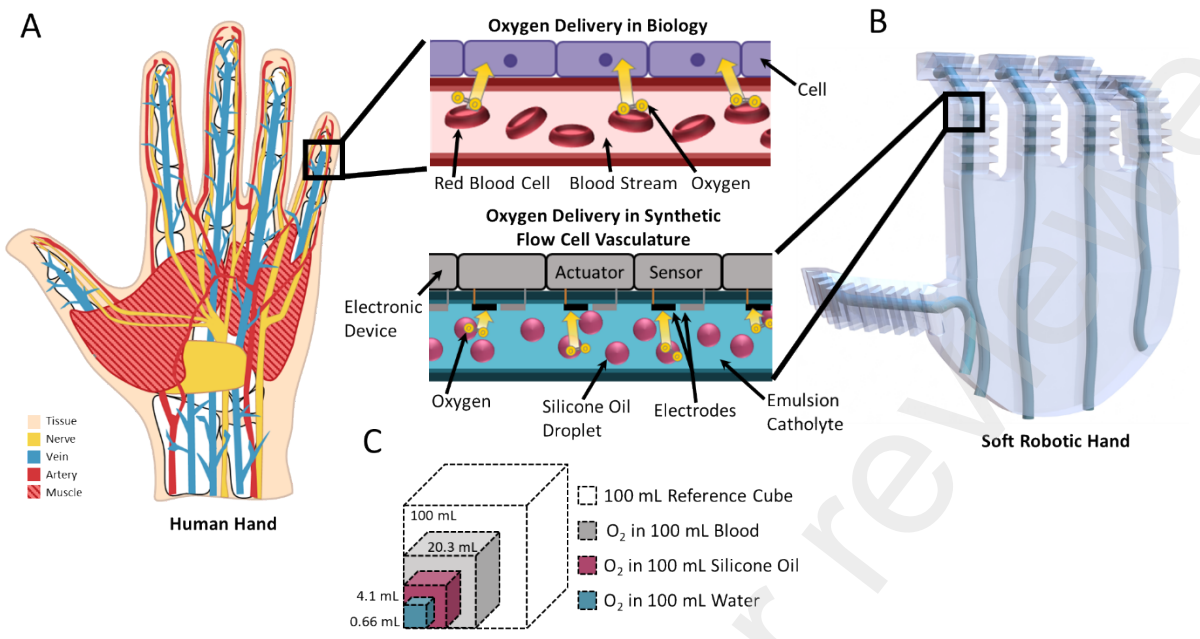

Figure 1. (A) Representation of the complex vasculature in a human hand. Detailed view of oxygen transport through the bloodstream for cellular respiration. (B) Representative soft robotic hand with synthetic, electrolytic vascular system. Detailed view of an integrated flow channel with an oxygenated liquid electrolyte used to power individual devices. (C) Comparison of volumetric oxygen solubility (per 100 mL) of blood, silicone oil, and water.

2. Materials and Methods

2.1 Emulsion Synthesis

Figure 2A depicts the silicone oil in water emulsion synthesis. We combined silicone oil (Thermo Fisher Scientific, 9990203) with 0.5M potassium hydroxide (KOH) in a ratio of 1:4 (v/v) followed by Span-60 (sorbitane monostearate, 1.0% w/v) surfactant to stabilize the interface. A sonic dismembrator (Fisherbrand Model 505) homogenized each 30 mL sample at an amplitude of 50 for 3 min (10 second pulses, 5s rest) to ensure uniform droplet dispersion and long-term stability. On average, samples received ~98 J/mL. Emulsion synthesis recipes with KOH salt concentrations higher than 0.5M demonstrated phase separation within a few hours of homogenization, so 0.5M KOH is used throughout this work.

2.2 Emulsion Characterization

Dynamic light scattering (DLS) on a Delsa Nano C Particle Analyzer (Beckman Coulter) measured the silicone oil droplet size distribution in diluted emulsion samples with 1 wt. % silicone oil. A scanning electron microscope (SEM; JEOL 7500F HRSEM) captured emulsion micrographs using an evaporation technique. We drop cast two microliters of a sample onto a carbon coated copper grid. After 2 minutes of evaporation, a wicking cloth eliminated excess liquid before imaging.

We created a dilution method inspired by previous work to measure the concentration of dissolved oxygen (DO) in the emulsions[36]. Figure 3A shows the apparatus, which allows the total oxygen stored in the silicone oil and water to be precisely measured by controlled release into a larger oxygen-free reservoir. First, we purged nitrogen (N_2) through a sealed measurement vial with 31.2 mL of distilled, deionized water while stirring at 800 RPM (stir bar 1 mm x 0.5 mm). An Orion Star A213 dissolved oxygen meter with an optical probe (ThermoFisher Scientific, Orion RDO Probe) measured the oxygen concentration in the measurement vial. The dissolved oxygen concentration of the water in the measurement vial typically reached a concentration of 0 mg/L after 20 minutes of purging with nitrogen. After purging the measurement vial for 35 minutes, we stopped the nitrogen flow, opened the valve, and dispensed 10.8 mL of the desired sample into the measurement vial at a flow rate of 31.8 mL/min while stirring continuously (800 RPM). The DO probe measured the oxygen concentration in the measurement vial over time as the oxygen from the emulsion sample diffused into the water (see Figure 3A). We validated this measurement method against a pure water control sample with saturated oxygen. The average error in the control sample between direct measurement with the probe and indirect measurement via the dilution method was 4.35%, which is within the range of reported error of the probe (~0.1 mg/L). Section S1 contains more information on the DO measurement protocol and validation.

2.3 Electrochemical Measurements

A biologic VMP3 potentiostat performed all electrochemical measurements. We conducted stationary linear sweep voltammograms (sweep rates: 50 mV/s, 100 mV/s, 200 mV/s) with a fully submerged Pt working electrode suspended via an electrochemically inert PTFE clamp (JJ110 electrode holder). The test setup used a carbon foil counter electrode and a mercury/mercury oxide (Hg/HgO) reference electrode (Koslow Scientific).

To measure the open circuit voltage and dissolved oxygen concentration of the same sample, we placed an emulsion sample in a sealed test vial with inlet and exhaust tubing to allow for purging with air or nitrogen (see Figure 3D). The three-electrode setup included a fully submerged Pt working electrode suspended via an electrochemically inert PTFE clamp, carbon foil counter electrode, and Hg/HgO reference electrode. We stirred the solution at 800 RPM for the duration of the experiment. At various intervals through the open circuit measurement, we extracted 15 mL of solution from the test vial to measure the dissolved oxygen concentration of the sample at that time point (see Figure 3A and 3D). The dissolved oxygen concentration was measured as described in *2.2*.

A rotation disk electrode (RDE; Pine Research) with a glassy carbon disk coated in a platinum carbon (Pt/C) ink served as the working electrode for RDE, kinetics, and catalysis measurements. To synthesize the Pt/C ink, we sonicated a mixture of 4 mg Pt on graphitized carbon (20 wt. %; Aldrich 739549), 0.8 mL water, and 0.2 mL ethanol for 15 minutes. We then added 10 µL of perfluorinated nafion resin solution and sonicated for an additional 2 minutes. We drop cast 10 µL of Pt/C ink onto the glassy carbon disk and dried it overnight. For RDE experiments, we placed 250 mL of emulsion or 0.5M KOH in an alkaline resistant PTFE test cell (Pine Research) and then perfused the solution with pure oxygen for 1.5 hours prior to testing such that both solutions would be fully saturated. We conducted linear sweep voltammograms for rotation disk

electrode studies at a sweep rate of 5 mV/s while rotating the electrode at rotation rates from 250 to 2500 RPM.

2.4 Flow Cell Assembly and Testing

We tested the discharge performance of ACEs in zinc-air flow cells with two different configurations, a stationary tubular flow cell (STFC) and a multifunctional actuator flow cell (MAFC). STFCs, shown in Figure 5A, use tubing both to house electrodes to form the structure of the flow cell and to circulate the ACE electrolyte throughout the cell. MAFCs, shown in Figure 5D, serve simultaneously as flow cells and actuators to demonstrate how ACEs can be used as multifunctional fluids for energy storage and hydraulic actuation.

The stationary tubular flow cell (STFCs) design was inspired by recent work on a submillimeter bundled microtubular (SBMT) flow battery cell[37]. STFCs were comprised of 1/8" ID plastic tubing (McMaster Carr, 9117T1), tee shaped barbed plastic tube fittings (McMaster Carr, 546K45), and high-temperature tapered plugs (McMaster Carr, 9277K18), as shown in Figure 5 and Figure S1. The cells had a 4 mg/cm^2 Pt black carbon cloth cathode (Fuel Cell Store), and a Zinc foil anode (Alfa Aesar, #10437). The separator was a PTFE coated alkaline anion exchange membrane (Dioxide Materials; E30-50). We used copper and zinc wires as the cathode and anode current collectors, respectively. We connected the electrodes through tee connectors on opposite sides of the main tubing, as shown in Figure S1 and described in Section S1. The additional two openings on the anode and cathode tee connectors served as inlet and outlet tubing connectors for the flow cell. A 24V DC peristaltic pump (McMaster, 33341N21) pumped the emulsion catholyte through the flow cell at a flow rate of 50 mL/min.

We assembled the multifunctional actuator flow cells (MAFCs) in a similar manner to STFCs with a notable difference being that the main tubing section was replaced with expandable tubing (Bellalatex twister balloon) encased in a plastic mesh sleeve (Mcmaster Carr, 5969K22) to form a McKibben actuator. We secured each end of the balloon mesh tubing to separate plastic barbed tube fittings (Mcmaster Carr, 5117K26) with a hose clamp (McMaster Carr, 5388K14). We connected the outlet tubing of the MAFC to a solenoid valve (12 V, Beduan) to automate the actuator inflation and deflation. We controlled the solenoid valve with a simple circuit and Arduino, as shown in Figure S2 and described in Section S1. For the demonstration video (Movie S2), we wired two MAFCs in series and used two solenoid valves and two peristaltic pumps, as shown in Figure S2.

3. Results and Discussion

Animal circulatory systems transport oxygen through complex vasculatures to deliver energy to various cells throughout the body. Ultimately, oxygen molecules diffuse from the blood stream into individual cells which derive energy by electrochemically reducing this oxygen through cellular respiration, as depicted in Figure 1A. Inspired by the vascular system's ability to continuously and simultaneously provide oxygen to the trillions of cells in the human body, we envision a soft robotic system with fully integrated, air-rechargeable energy delivery and storage. Figure 1B shows a representative illustration of this concept using a soft robotic hand with flow channels filled with a multifunctional fluid (shown in teal) that simultaneously transports energy and hydraulically actuates the fingers (see Figure 1B). This multifunctional fluid can transport dissolved oxygen throughout the soft hand and deliver oxygen locally at integrated internal electrodes to power various individual electronic devices, as depicted in the vascular cross-section in Figure 1B, or provide a continuous supply of gas for other chemical or mechanical functions.

Realizing an ionically conducting fluid capable of storing large amounts of dissolved oxygen is a fundamental first step toward creating this fully integrated energy transport system. Higher concentrations of dissolved oxygen in the electrolyte increase the reaction rate of oxygen reduction[19], allow larger energy flux, and increase the number of components that can be powered before the oxygen needs to be recharged. Figure 1C schematically compares the solubility of oxygen in human blood (20.3 mL/100 mL at 37°C internal body temperature), silicone oil (4.11 mL/100 mL, 21°C), and pure water (0.664 mL/100 mL, 21°C) (also see Table S1). Volumetrically, human blood contains 30 times as much oxygen as water. Water has a low oxygen solubility (8.8 mg/L; 0.0066 mL O_2/mL water) which decreases as the concentration of dissolved ions increases. Air-saturated silicone oil can store 6.2 times as much dissolved oxygen as pure water, but silicone oil is not ionically conductive.

We combined silicone oil with potassium hydroxide (KOH) electrolyte to create an emulsion where silicone oil droplets were suspended and uniformly dispersed throughout the aqueous phase, as graphically depicted in Figure 1B. The oil phase of the emulsion stored oxygen at high concentrations while the aqueous phase allowed the ionic mobility necessary for electrochemical reactions. This silicone oil-in-water emulsion served as an air catholyte emulsion (ACE) for ORR and can be used in metal-air batteries or fuel cells.

3.1 Emulsion Properties

To maintain uniform oxygen distribution and fast kinetics, it is important that emulsions remain stable and do not phase separate. Figure 2B shows a scanning electron microscope (SEM) image of an emulsion shortly after synthesis following the procedure in *2.1* and *2.2*. The SEM image provides an initial estimate of oil droplet diameters and droplet size distributions, demonstrating ~300 nm droplet diameters. Figure 2C shows optical images of an emulsion sample

that was left to rest undisturbed for 365 days. The uniform, milky color of the sample on Day 0 indicates that a colloidal suspension was formed. After 7 days, the sample retained uniform coloration with no visible phase separation or sedimentation. After 60 days and 365 days, there was slight sedimentation, as can be seen by the lighter color at the bottom of the vial (see section S2). However, the sample retained its milky color indicating no distinct phase separation. This form of a stability test is a conservative shelf-life estimate, as the envisioned use case for the ACE involves continuous convection in a flow cell setup, which would mix the solution to maintain a uniform dispersion.

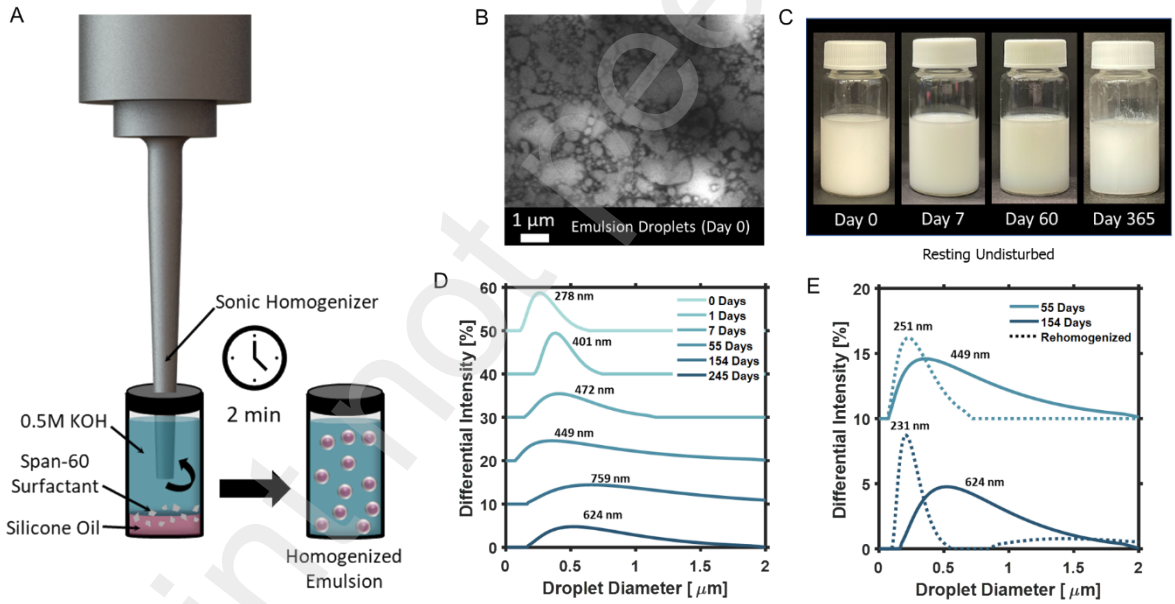

Figure 2. (A) Schematic representation of the emulsion synthesis process. (B) Scanning electron microscope (ESEM) image of emulsion captured shortly after synthesis. (C) Optical images of an emulsion sample resting undisturbed for up to 365 days since synthesis. (D) Dynamic light scattering (DLS) measurements comparing the droplet diameter of different emulsion samples which remained stirring from synthesis until testing. The differential intensity axis is purposefully offset for visibility. (E) DLS measurements comparing the average droplet diameter of emulsion samples before and after a re-homogenization procedure. The differential intensity axis is purposefully offset for visibility.

Dynamic light scattering (DLS) measurements show the distribution of silicone oil droplet diameters in the emulsion over a 250-day period. Figure 2D compares DLS differential intensity as a function of droplet diameter for several different emulsion samples at various time points post-synthesis. All samples were stored under continuous magnetic stirring (~500 RPM) until they were diluted to perform the DLS measurement. This stirring served to mimic the convection that would occur if the ACE were to be continuously used in a flow cell. As shown in Figure 2D, the peak droplet diameter for an as-synthesized emulsion (Day 0) was 278 nm. Over time, droplets agglomerated under continuous stirring, as shown by the increasing peak droplet diameter as the time from synthesis increases. Further, the width of the differential intensity peak is correlated with the uniformity of the droplet diameters. As shown in Figure 2D, as-synthesized emulsions have sharper peaks, demonstrating a more uniform dispersion of silicone oil droplets. While the peak droplet diameter remains similar (< 20% change) from 1 day post synthesis up to 55 days post synthesis, peaks become gradually more diffuse as time post synthesis increases. This demonstrates that droplet diameter uniformity decreases as the time post synthesis increases.

While droplet agglomeration occurs over time, this process is reversible. Re-homogenizing an older sample restores smaller, more uniformly dispersed droplets. Figure 2E compares the differential intensity as a function of droplet diameter for two different emulsion samples, one tested 55 days after synthesis and one tested 154 days after synthesis. The solid lines indicate the intensity data of the sample that was under continuous stirring from synthesis until DLS testing. The dotted lines show differential intensity data for the same sample that was re-homogenized prior to testing. After re-homogenization, the peak droplet diameter for both samples decreased and was comparable to that of the freshly synthesized sample shown in Figure 2D. Additionally, the peak sharpened after re-homogenization, indicating a more uniform droplet dispersion. Our

silicone oil emulsions demonstrate droplet agglomeration over time; however, low droplet diameters can be regenerated from old samples.

We measured the dissolved oxygen (DO) concentration in the emulsions to test our hypothesis that adding silicone oil will increase the emulsion DO because silicone oil can dissolve 6.2 times as much oxygen as water, by volume. The emulsion samples synthesized in this work were 20% silicone oil by volume, which lead to an expected DO concentration of 16.5 mg/L. Since DO meters can only directly measure the DO concentration in aqueous solutions, we used a dilution method to measure the DO concentration in our emulsion samples, as described in *2*.2 and depicted in Figure 3A. First, a vial of water (31.2 mL) was pre-purged with N_2 until it reached a concentration of 0 mg/L oxygen. Then, a small amount (10.8 mL) of the desired sample was introduced into the measurement vial while continuously stirring. Oxygen from the emulsion samples diffused into the water at a concentration below the saturation limit. A DO meter then measured the increase in oxygen in the water over time. This DO measurement protocol was validated across different known conditions as described in Section S1 and shown in Figure S3.

Figure 3B compares the concentration of dissolved oxygen in our emulsion samples to that of pure water and 0.5M KOH. Table S1 compares the gravimetric and volumetric dissolved oxygen concentration for the various media referenced throughout this work. The data in Figure 3B is the average value across three trials for a given fluid. The DO data for individual trials can be seen in Figure S3. The DO concentration of 0.5M KOH (7.6 mg/L) was less than that of pure water (8.8 mg/L). The 80% KOH emulsion samples stored 1.9 times the dissolved oxygen (14.6 mg/L) as the pure KOH samples. Figure 3C schematically compares the measured volumetric dissolved oxygen concentration in our emulsions to 0.5M KOH relative to a 100 mL reference cube. Emulsions retain their high dissolved oxygen concentration for several months. Figure 3B shows that the

dissolved oxygen concentration for an emulsion sample 195 days post-synthesis (14.6 mg/L) was the same as the reference emulsion sample. The 195-day old emulsion sample was kept in a closed container to prevent evaporation and gas transfer and under continuous stirring to mimic a flow battery use case. Emulsion samples can dissolve large amounts of oxygen and maintain these high oxygen levels over time.

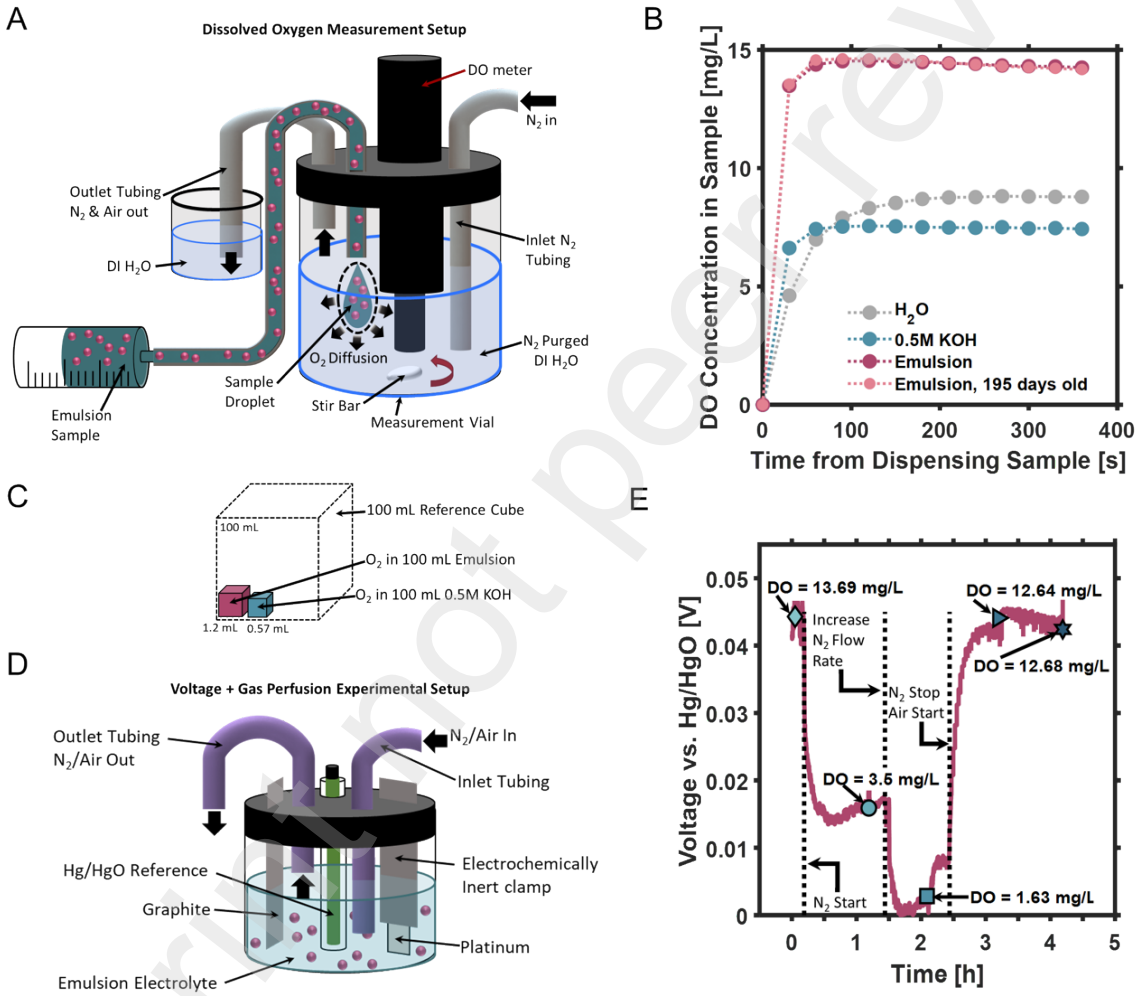

Figure 3. (A) Schematic representation of experimental setup for measuring the amount of dissolved oxygen in emulsions. (B) Average (n = 3) dissolved oxygen concentrations for water, 0.5M KOH, and emulsions at 21°C. (C) Comparison of volumetric dissolved oxygen measurements (per 100 mL) of water, 0.5M KOH, and emulsions. (D) Schematic representation of experimental setup for measuring the open circuit volage and dissolved oxygen concentration of a sample. (E) Open circuit voltage (vs. Hg/HgO) and dissolved oxygen concentration data for an emulsion sample that was perfused with nitrogen and air to demonstrate the capability of an emulsion to be recharged via air perfusion.

The ability to store and retain oxygen makes silicone oil emulsions a suitable candidate for air catholytes. Once all the dissolved oxygen in the air emulsion catholyte has been consumed, oxygen needs to be extracted from surrounding air to effectively recharge the ACE. Figure 3E correlates the open circuit voltage of an ACE with its dissolved oxygen concentration over time. Figure 3D shows a schematic representation of the experimental setup used to control the amount of dissolved oxygen in an ACE while measuring the open circuit voltage (OCV). For this measurement, the Platinum working electrode is completely submerged in the emulsion such that the only oxygen available for ORR is the oxygen dissolved in the sample. Initially, the ACE is saturated with dissolved oxygen (13.7 mg/L) and rests at an OCV of 0.044V vs. Hg/HgO. The ACE was then purged with N_2 to displace any dissolved oxygen and mimic a flow battery that has consumed all available dissolved oxygen during discharge. After perfusing with nitrogen for one hour, the OCV decreased to 0.016V and the DO concentration decreased to 3.5 mg/L (75% decrease). The flow rate of N_2 into the ACE was then increased and perfusion continued. An additional ~1 hour of purging with nitrogen yielded another decrease in OCV (0.0028 V) and corresponding decrease in DO concentration down to 1.6 mg/L. After completely purging the ACE with N_2, the sample was perfused with air to simulate recharging of oxygen the from the surroundings. Immediately after the air flow started, the OCV showed a steep increase toward the initial starting voltage. After 0.75 hours of air perfusion, both dissolved DO concentration (12.6 mg/L) and OCV (0.044 V) had returned to their starting values. Additional air perfusion showed little change in both OCV and DO concentration. Figure 3E demonstrates that silicone oil emulsions can be recharged via air perfusion and are good candidates for air-rechargeable flow battery catholytes.

3.2 Electrochemical Performance

The air-catholyte emulsion has superior oxygen reduction reaction kinetics than 0.5 M KOH electrolyte with fully submerged electrodes. Figure 4A compares stationary linear sweep voltammogram (LSV) curves for oxygen-saturated 0.5 KOH emulsions and pure 0.5M KOH electrolytes with a fully submerged platinum working electrode. The emulsion curve shows a well-defined reduction peak, indicating the occurrence of oxygen reduction, and demonstrates 4.9 times the peak current density as the 0.5M KOH electrolyte. This trend is independent of scan rate, as shown in Figure S4.

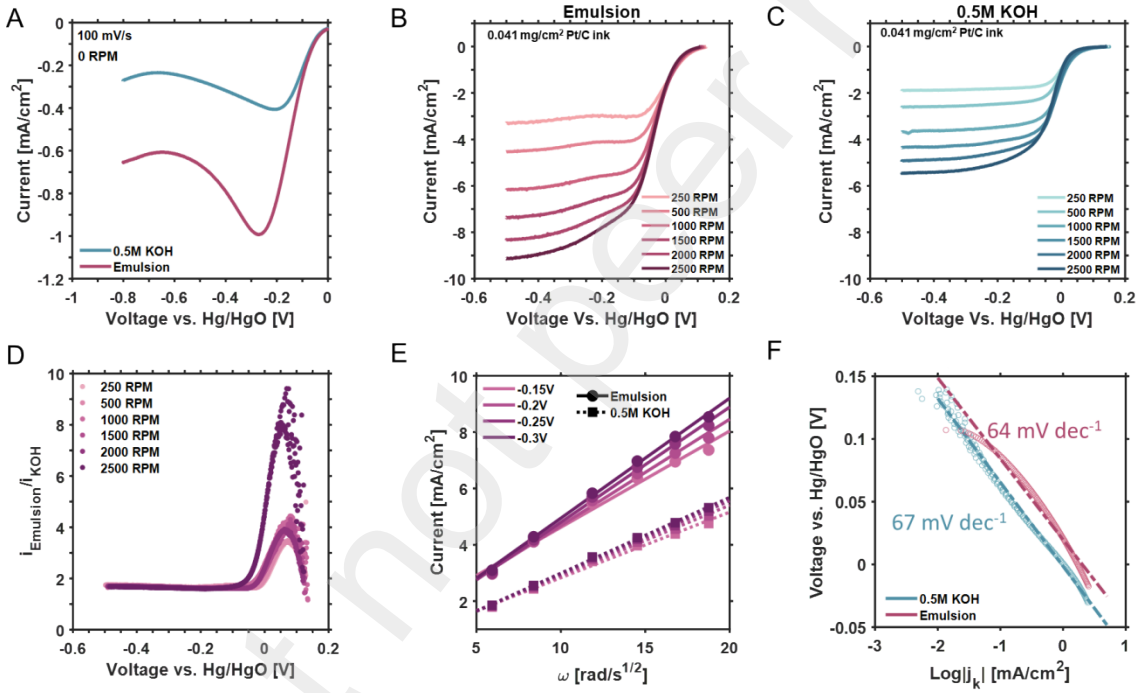

Figure 4. (A) Stationary linear sweep voltammogram scans with a submerged platinum electrode at a scan rate of 100 mV/s comparing the oxygen reduction peak in an O_2-saturated 0.5M emulsion sample to a 0.5M KOH sample. Linear sweep voltammogram scan curves of Pt/C ink on a glassy carbon rotating disk electrode in O_2-saturated (B) 0.5M KOH emulsion and (C) 0.5M KOH samples at a scan rate of 5 mV/s. (D) Ratio of oxygen reduction current in emulsion to 0.5M KOH as a function of voltage (E) Levich plot of current versus square root of rotation rate ($\omega^{1/2}$) for emulsion and 0.5M KOH samples. (F) Tafel plots of Pt/C ink in emulsions and 0.5M KOH samples.

To further characterize the catalytic activity and ORR kinetics in the emulsions compared to a pure KOH electrolyte, we conducted rotation disk electrode (RDE) experiments with oxygen saturated electrolytes at a voltage sweep rate of 5 mV/s and disk rotation rates ranging from 250-

2500 RPM. Figure 4B and C depict LSV sweeps at different rotation rates for a 0.5M KOH emulsion and 0.5M KOH electrolyte. The emulsion has a higher current than potassium hydroxide across all rotation rates, indicating higher ORR catalytic activity. We attribute this high ORR activity to the high dissolved oxygen concentration in the emulsions, which might surpass the saturation limit of the KOH electrolyte near the silicone oil interfaces. Figure 4D plots the ratio of measured current in the 0.5M KOH emulsion scans (as seen in Figure 4B) to 0.5M KOH scans (as seen in Figure 4C) at various RDE rotation rates. Rotation rates below 2500 RPM experience similar current ratio peaks ranging from 3.5-4.4. At these lower rotation rates, the current ratio reaches its peak of 4.4 at 0.07V. This early peak in the current ratio is because the emulsion shows an earlier onset potential than the KOH electrolyte. This can be seen more clearly in Figure S5, which directly compares RDE voltammograms between the emulsion and KOH at selected scan rates. At 0.07V, where the current ratio peak occurs, emulsion scans show a steep increase in current while KOH scans are still in the baseline current plateau region of the sigmoid wave. As the voltage decreases toward the area where diffusion limiting current exists on the RDE voltammograms, the current ratio for all rotation rates converges to 1.7 (see Figure 4B and C). This indicates that the diffusion limited current for 0.5M KOH emulsions is 1.7 times that of 0.5M KOH.

Figure 4E shows Levich plots at different potentials for both electrolytes. The expected linear dependence holds for both emulsions and KOH electrolytes, indicating first order kinetics with respect to oxygen. Figure 4F compares Tafel plots for emulsion and KOH electrolytes. The two electrolytes have comparable Tafel slopes, though the emulsion has the lower slope (64 mV/decade), indicating faster ORR kinetics in 0.5M KOH emulsions compared to 0.5M KOH.

Overall, Figure 4 demonstrates that air-catholyte emulsions have excellent oxygen reduction kinetics, even when the working electrode is not in direct contact with air.

3.3 Stationary Tubular Flow Cells and Multifunctional Actuator Flow Cells

To test the performance of air emulsion catholytes in a full electrochemical cell, we created a stationary tubular flow cell (STFC). Figure 5A shows the experimental setup for assembling an STFC. Additional details are described in *2.4*. Inspired by recent work,[37] the STFC eliminates the need for traditional flow cell setups which are prone to leaks and often require high stack pressure. This design incorporates electrodes into the tubing itself, decreasing overall cell volume and creating a more flexible full cell. Our STFCs have a platinum carbon cloth cathode and pure zinc anode, separated by a PTFE-backed alkaline anion exchange membrane. The ACE is pumped through the flow cell via a peristaltic pump (50 mL/min) and recycled continuously. The inset image in Figure 5A shows a fully assembled STFC without the inlet and outlet tubing connected.

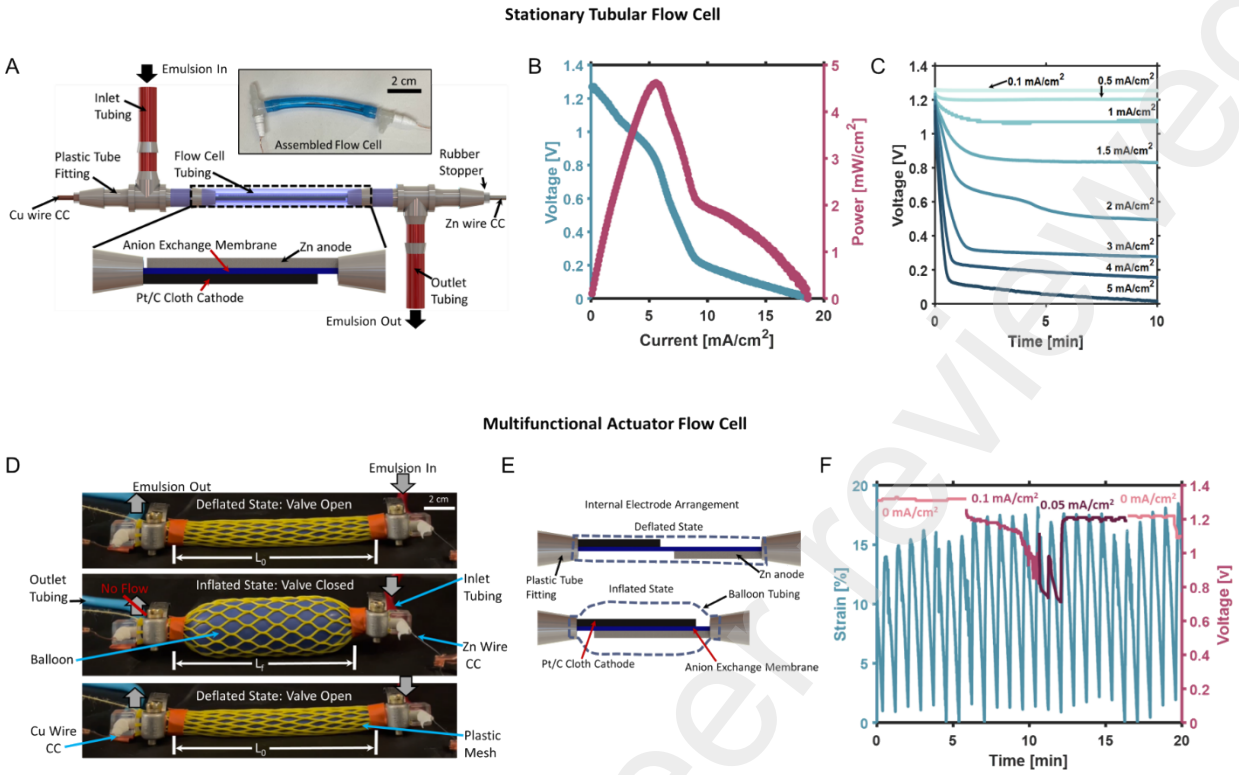

Figure 5. (A) Diagram of stationary tubular flow cell (STFC) showing inlet and outlet for the pumped emulsion electrolyte, Pt/C cloth cathode, anion exchange membrane separator, Zinc anode and current collectors. Inset: Optical image of an assembled flow cell. (B) Electrode polarization (left axis, teal) and power (right axis, burgundy) curves (50 µA/s scan rate) for a STFC with an emulsion catholyte pumped at 50 mL/min. (C) Discharge profiles for a STFC with an emulsion catholyte pumped at 50 mL/min, discharged at various current densities. (D) Optical images of a multifunctional actuator flow cell (MAFC) at three different actuation states. (E) Schematic showing the internal electrode placement for a MAFC in an inflated and deflate sate. (F) Strain (left axis, teal) and voltage (right axis, burgundy) data for a MAFC with an emulsion catholyte pumped at 50 mL/min discharged at various current densities.

Figure 5B shows polarization and power curves for an STFC. The STFC achieves an instantaneous peak power of 4.6 mW/cm^2 at a current density of 5.6 mA/cm^2. The polarization curve shows three distinct linear regions, with the largest voltage drop occurring in the middle linear region. Significant losses within the STFC are attributed to ohmic resistance in the cell. The Nyquist impedance plot for this STFC has a real intercept of 40 ohms, indicating a high bulk resistance (see Figure S6) attributed to a lack of external pressure within the STFC which increases contact resistance and the separation distance between the anode and cathode within the flow cell

tubing. Figure S8 compares the bulk solution resistance of various electrolytes tested in a controlled coin cell setup and shows opportunities for impedance improvements with higher pressure and higher concentration electrolytes (see Section S4).

Figure 5C shows a discharge rate study for the STFC discharged from 0.1 mA/cm^2 up to 5 mA/cm^2. Low discharge currents yield minimal voltage losses and steady discharge plateaus. At a discharge rate of 0.1 mA/cm^2 a steady voltage plateau of 1.25V is maintained for the entire 10-minute discharge. Similarly, 0.5 mA/cm^2 and 1 mA/cm^2 discharge rates yield steady discharge voltage of 1.2V and 1.1V, respectively. At 1.5 mA/cm^2, the cell shows a larger initial voltage drop, but the discharge plateau remains constant at 0.84V. At higher current densities, additional losses are observed. At 5 mA/cm^2, the flow cell voltage drops to 0.13V in less than one minute, which is impractical for most applications. Figure S9 shows a pseudo polarization and power graph generated from the discharge data in Figure 5C. The average voltage and power from each individual discharge experiment are plotted vs. the discharge current to elucidate the power and voltage performance of a cell under continuous, rather than instantaneous discharge conditions. The average discharge power density of the STFC reaches a maximum of 1.3 mW/cm^2 at a discharge current density of 1.5 mA/cm^2. Discharging the STFC at rates of 1, 2.5, 3, and 3.5 would all yield a sustained average power density of ~1 mW/cm^2.

To collect the data from Figure 5C, the STFC voltage was continuously measured as each discharge was followed by an OCV rest period and then the next higher-rate discharge, as can be seen in FigureS10A-C. Not only does Figure S10 demonstrate that ACEs could be well suited for longer continuous use, but it also shows that the current-induced voltage losses seen in Figure 5C are recoverable. At a certain point, either the zinc anode or all the dissolved oxygen in the ACE will be consumed. Until this limit, the losses endured by the STFC are reversible. Figure S10D-F

shows the power performance of an STFC during this 250 min discharge rate study. The STFC achieves a maximum sustained power of 1.25 mW/cm^2 (at 1.5 mA/cm^2) and a maximum instantaneous power of 5.2 mW/cm^2 at the beginning of the 4.5 mA/cm^2 discharge.

Finally, to demonstrate that ACEs are well suited for fully integrated multifunctional energy storage, we created a multifunctional actuator flow cell (MAFC) which can simultaneously hydraulically actuate and produce electrical energy. Figure 5D shows the MAFC setup, which is similar to the STFC but the main cell tubing was replaced by stretchable tubing encased in a rigid, plastic mesh to create a McKibben actuator. The plastic mesh constrains the expansion of the inner tubing to one-dimensional actuation along the tube length. The series of images in Figure 5D shows the MAFC as it is actuated from its initial length to its final length and then returns to its original length (see Movie S1). This actuation was achieved by inflating the inner flexible tubing with the ACE which serves both as an energy storage and hydraulic fluid. The MAFC is connected to inlet and outlet tubing and a peristaltic pump continuously pumps the ACE through the cell. At the outlet, a solenoid valve controls whether there is outflow of fluid from the MAFC. When the valve is closed, the MAFC inflates and the total length decreases. When the valve is opened, the MAFC deflates and returns to its original length. Since the MAFC design has each electrode inserted from either end of the tubing, the distance between the electrodes is a function of the actuation state of the MAFC. Figure 5E shows the internal electrode structure inside the MAFC during two different actuation states, fully deflated (top), and fully inflated (bottom). The fully deflated state shows no electrode overlap while the fully inflated state has maximum electrode overlap and thus minimum distance between electrodes. Since the ohmic resistance of the cell increases with increasing distance between electrodes, it is expected that the discharge performance of the MAFC is worse when inflated, as the electrodes are farthest apart in this state.

Figure 5F shows an overlay of strain and voltage data for an MAFC which is simultaneously actuating and discharging. The strain data (left axis, teal), shows stable and repeatable cycling, up to a maximum strain of 18% for 23 cycles. The discharge data (Fig. 5F right axis, shades of burgundy) shows the voltage performance of an MAFC under 3 different applied current conditions. Initially, the cell is in an open-circuit rest period (0 mA/cm^2) with an initial cell voltage of 1.32 V. The cell is then discharged at a current density of 0.1 mA/cm^2 where it experiences a gradual decline voltage to 1.12V over 3 minutes. After this initial gradual voltage decrease, the cell experiences a steep voltage drop (0.8V) until the discharge current decreases to 0.05 mA/cm^2. The STFC discharged at the same rate (0.1 mA/cm^2) showed a stable voltage plateau of 1.25V. We attribute the poor rate performance of the MAFC to the ohmic resistances which result from the large separation distance between electrodes (see Figure 5E). Once the discharge current is decreased to 0.05 mA/cm^2, the MAFC voltage shows some oscillating dips and increases over the first 2 minutes before returning toward the initial open circuit voltage (OCV) and remaining stable at 1.21V for the remaining 4 minutes. The slight voltage oscillations that can be seen during the 0.05 mA/cm^2 discharge and final rest period are likely an artifact of the electrode distance changing as the MAFC actuates. A final OCV rest period shows that the MAFC can restore its initial voltage (1.22V). The MAFC discharge data demonstrates that current-induced voltage losses in emulsion catholytes are reversible with the introduction of lower current or full rest periods. Movie S2 and Figure S2 show two MAFCs with offset actuation states wired in series to light up an LED. This setup illustrates how multiple MAFCs could work together when integrated into a device.

4. Conclusions

This work demonstrates silicone oil-based air catholyte emulsions for flow batteries with fully submerged electrodes. Inspired by biological circulatory systems which transport and deliver dissolved oxygen through complex networks, we created an ACE capable of storing large amounts of dissolved oxygen (15.8 mg/L). Emulsions can maintain a uniformly dispersed oil phase and remain saturated with oxygen for several months. 0.5M KOH emulsions exhibit fast oxygen reduction reaction kinetics with fully submerged electrodes, with twice as much diffusion limiting current as a control 0.5M KOH electrolyte. ACEs can achieve a maximum instantaneous power density of 4.6 mW/cm^2 at 5.6 mA/cm^2 and can produce 1.2 mW/cm^2 of sustained power at a discharge current density of 1.5 mA/cm^2 in a zinc-air flow cell configuration where the only available oxygen is dissolved in the emulsion. Significant voltage losses, largely due to high resistances in the STFC, occur at discharge current densities above 2 mA/cm^2; however, these voltage losses are recoverable after a short rest period if the dissolved oxygen in the ACE has not yet been depleted. Once depleted, ACEs can be re-saturated and thus recharged with an influx of surrounding air. Air emulsion catholytes are well suited for high energy density flow battery systems because they can extract energy from their surroundings but without the need for a semi-open system like traditional air batteries.

As this work presents an initial demonstration of the ACE concept, further optimization of both the emulsion and the flow cell design should yield higher power density and better rate performance. The emulsion synthesis recipe, specifically the ratio of silicone oil to aqueous phase as well as the ion choice and concentration in the aqueous phase is a promising area for further study. Increasing the ratio of silicone oil in emulsions should increase the amount of dissolved oxygen, but at the expense of ionic conductivity. Increasing concentration of ions in solution in the aqueous phase should improve the conductivity but will eventually inhibit the emulsions

stability. The ohmic losses present in STFCs and MAFCs can be mitigated both by increasing the bulk conductivity of the emulsion but also by a more optimal cell design with minimal transport distances between electrodes.

ACE is a first step towards integrating soft robotic systems with multifunctional, high-energy, air-rechargeable energy storage. Autonomous robotic systems designed with multifunctional components experience higher system-level efficiency. Energy storage components should be designed and implemented as multifunctional components in the systems that they power. In addition, the human body is continuously providing oxygen to its trillions of cells for cellular respiration without the need for each individual cell to have access to the surrounding air. We hope to embody future robotic systems with this same capability where many individual components can simultaneously extract oxygen from a distributed fluid.

ASSOCIATED CONTENT

Supporting Information

Additional experimental details, materials, and methods (PDF)
Multifunctional Actuator Flow Cell Strain Demonstration (mp4)
Two Multifunctional Actuator Flow Cells (mp4)

AUTHOR INFORMATION

Corresponding Author

James H. Pikul – Department of Mechanical Engineering, University of Wisconsin-Madison Madison, WI 53706, United States of America

**email: jpikul@wisc.edu*

Present Addresses

†If an author's address is different than the one given in the affiliation line, this information may be included here.

Author Contributions

The manuscript was written through contributions of all authors. All authors have given approval to the final version of the manuscript.

ACKNOWLEDGMENT

This work was carried out in part at the Singh Center for Nanotechnology, which is supported by the NSF National Nanotechnology Coordinated Infrastructure Program under grant NNCI-2025608. This research was funded by the National Science Foundation CAREER Award #2344714 and GRFP Award #1845298. This research was also supported in part by the Office of Naval Research N000142212569. Muqing Ren, Jamie Ford, and Joseph Rosenfeld also supported this work.

ABBREVIATIONS

ACE	Air Emulsion Catholyte
DLS	Dynamic Light Scattering
DO	Dissolved Oxygen
EIS	Electrochemical Impedance Spectroscopy
LSV	Linear Sweep Voltammogram
MAFC	Multifunctional Actuator Flow Cell

OCV	Open Circuit Voltage
ORR	Oxygen Reduction Reaction
RDE	Rotation Disk Electrode
SEM	Scanning Electron Microscope
STFC	Stationary Tubular Flow Cell

REFERENCES

(1) Erdosy, D. P.; Wenny, M. B.; Cho, J.; DelRe, C.; Walter, M. V.; Jiménez-Ángeles, F.; Qiao, B.; Sanchez, R.; Peng, Y.; Polizzotti, B. D.; de la Cruz, M. O.; Mason, J. A. Microporous Water with High Gas Solubilities. *Nat. 2022 6087924* **2022**, *608* (7924), 712–718.

(2) Thorarinsdottir, A. E.; Erdosy, D. P.; Costentin, C.; Mason, J. A.; Nocera, D. G. Enhanced Activity for the Oxygen Reduction Reaction in Microporous Water. *Nat. Catal. 2023 65* **2023**, *6* (5), 425–434.

(3) Kronberger, H.; Bruckner, K.; Fabjan, C. Reduction of Oxygen from Electrolyte Emulsions with High Oxygen Contents. *J. Power Sources* **2000**, *86* (1), 562–567.

(4) Bisht, M.; Bhawna; Singh, B.; Pandey, S. Deep Eutectic Solvent-Modified Mesoporous Silica for CO2 Capture: A New Generation of Hybrid Sorbents. *J. Mol. Liq.* **2023**, *384*, 122203.

(5) Ma, J.; He, L.; Yang, R.; Wang, D.; Qu, D.; Su, C.; Pang, H.; Wu, W.; Li, P.; Zhang, L.; Liu, X. Porous Liquid Metal-Organic Frameworks with Selectively High Gas Solubility. *Fuel* **2023**, *344*, 128051.

(6) Mainar, A. R.; Iruin, E.; Colmenares, L. C.; Kvasha, A.; de Meatza, I.; Bengoechea, M.; Leonet, O.; Boyano, I.; Zhang, Z.; Blazquez, J. A. An Overview of Progress in Electrolytes for Secondary Zinc-Air Batteries and Other Storage Systems Based on Zinc. *J. Energy Storage* **2018**, *15*, 304–328.

(7) Tian, W. W.; Ren, J. T.; Lv, X. W.; Yuan, Z. Y. A "Gas-Breathing" Integrated Air Diffusion Electrode Design with Improved Oxygen Utilization Efficiency for High-Performance Zn-Air Batteries. *Chem. Eng. J.* **2022**, *431*, 133210.

(8) Zhang, Q.; Zhou, M.; Ren, G.; Li, Y.; Li, Y.; Du, X. Highly Efficient Electrosynthesis of Hydrogen Peroxide on a Superhydrophobic Three-Phase Interface by Natural Air Diffusion. *Nat. Commun.* **2020**, *11* (1), 1731.

(9) Tang, C.; Wang, H. F.; Zhang, Q. Multiscale Principles to Boost Reactivity in Gas-

Involving Energy Electrocatalysis. *Acc. Chem. Res.* **2018**, *51* (4), 881–889.

(10) Moni, P.; Deschamps, A.; Schumacher, D.; Rezwan, K.; Wilhelm, M. A New Silicon Oxycarbide Based Gas Diffusion Layer for Zinc-Air Batteries. *J. Colloid Interface Sci.* **2020**, *577*, 494–502.

(11) Ozden, A.; Shahgaldi, S.; Li, X.; Hamdullahpur, F. A Review of Gas Diffusion Layers for Proton Exchange Membrane Fuel Cells—With a Focus on Characteristics, Characterization Techniques, Materials and Designs. *Prog. Energy Combust. Sci.* **2019**, *74*, 50–102.

(12) An, T.; Ge, X.; Tham, N. N.; Sumboja, A.; Liu, Z.; Zong, Y. Facile One-Pot Synthesis of CoFe Alloy Nanoparticles Decorated N-Doped Carbon for High-Performance Rechargeable Zinc-Air Battery Stacks. *ACS Sustain. Chem. Eng.* **2018**, *6* (6), 7743–7751.

(13) Zhao, Z.; Liu, B.; Fan, X.; Liu, X.; Ding, J.; Hu, W.; Zhong, C. An Easily Assembled Boltless Zinc–Air Battery Configuration for Power Systems. *J. Power Sources* **2020**, *458*, 228061.

(14) Gao, Y.; Pan, Z.; Sun, J.; Liu, Z.; Wang, J. High-Energy Batteries: Beyond Lithium-Ion and Their Long Road to Commercialisation. *Nano-Micro Lett. 2022 141* **2022**, *14* (1), 1–49.

(15) Zhao, Z.; Liu, B.; Fan, X.; Liu, X.; Ding, J.; Hu, W.; Zhong, C. Methods for Producing an Easily Assembled Zinc-Air Battery. *MethodsX* **2020**, *7*, 100973.

(16) Yu, W.; Shang, W.; Tan, P.; Chen, B.; Wu, Z.; Xu, H.; Shao, Z.; Liu, M.; Ni, M. Toward a New Generation of Low Cost, Efficient, and Durable Metal–Air Flow Batteries. *J. Mater. Chem. A* **2019**, *7* (47), 26744–26768.

(17) Chen, P.; Zhang, K.; Tang, D.; Liu, W.; Meng, F.; Huang, Q.; Liu, J. Recent Progress in Electrolytes for Zn–Air Batteries. *Front. Chem.* **2020**, *8*, 372..

(18) Chen, X. J.; Shellikeri, A.; Wu, Q.; Zheng, J. P.; Hendrickson, M.; Plichta, E. J. A High-Rate Rechargeable Li-Air Flow Battery. *J. Electrochem. Soc.* **2013**, *160* (10), A1619–A1623.

(19) Meng, R.; Zhang, C.; Lu, Z.; Xie, X.; Liu, Y.; Tang, Q.; Li, H.; Kong, D.; Geng, C. N.; Jiao, Y.; Fan, Z.; He, Q.; Guo, Y.; Ling, G.; Yang, Q. H. An Oxygenophilic Atomic Dispersed Fe-N-C Catalyst for Lean-Oxygen Seawater Batteries. *Adv. Energy Mater.* **2021**, *11* (23), 2100683.

(20) Aubin, C. A.; Gorissen, B.; Milana, E.; Buskohl, P. R.; Lazarus, N.; Slipher, G. A.; Keplinger, C.; Bongard, J.; Iida, F.; Lewis, J. A.; Shepherd, R. F. Towards Enduring Autonomous Robots via Embodied Energy. *Nat. 2022 6027897* **2022**, *602* (7897), 393–402.

(21) Aubin, C. A.; Choudhury, S.; Jerch, R.; Archer, L. A.; Pikul, J. H.; Shepherd, R. F. Electrolytic Vascular Systems for Energy-Dense Robots. *Nature* **2019**, *571* (7763), 51–57.

(22) Clark, L. C.; Gollan, F. Survival of Mammals Breathing Organic Liquids Equilibrated with Oxygen at Atmospheric Pressure. *Science (80-.).* **1996**, *152* (3730), 1755–1756.

(23) Leung, R.; Poncelet, D.; Neufeld, R. J. Enhancement of Oxygen Transfer Rate Using Microencapsulated Silicone Oils as Oxygen Carriers. *J. Chem. Technol. Biotechnol.* **1997**, *68* (1), 37–46.

(24) Dumont, E.; Andrès, Y.; Le Cloirec, P. *Enhancement of Oxygen Transfer in Bioprocesses by the Use of an Organic Phase: Effect of Silicone Oil on Volumetric Mass Transfer Coefficient of Oxygen*; 2005.

(25) Quijano, G.; Revah, S.; Gutiérrez-Rojas, M.; Flores-Cotera, L. B.; Thalasso, F. Oxygen Transfer in Three-Phase Airlift and Stirred Tank Reactors Using Silicone Oil as Transfer Vector. *Process Biochem.* **2009**, *44* (6), 619–624.

(26) Chibata, I.; Yamada, S.; Wada, M.; Izou, N.; Yamaguchi, T. Cultivation of Aerobic Microorganisms. 3,850,753, March 13, 1973.

(27) Xu, A.; He, B.; Yu, H.; Han, W.; Li, J.; Shen, J.; Sun, X.; Wang, L. A Facile Solution to Mature Cathode Modified by Hydrophobic Dimethyl Silicon Oil (DMS) Layer for Electro-Fenton Processes: Water Proof and Enhanced Oxygen Transport. *Electrochim. Acta* **2019**, *308*, 158–166.

(28) Ji, M. B.; Wei, Z. D.; Chen, S. G.; Li, L. A Novel Antiflooding Electrode for Proton Exchange Membrane Fuel Cells. *J. Phys. Chem. C* **2009**, *113* (2), 765–771.

(29) Zhang, F.; Chen, G.; Hickner, M. A.; Logan, B. E. Novel Anti-Flooding Poly(Dimethylsiloxane) (PDMS) Catalyst Binder for Microbial Fuel Cell Cathodes. *J. Power Sources* **2012**, *218*, 100–105.

(30) Ji, M. B.; Wei, Z. D.; Chen, S. G.; Xia, M. R.; Zhang, Q.; Qi, X. Q.; Hu, X. H.; Ding, W.; Li, L. Electrochemical Impedance Spectroscopy Evidence of Dimethyl-Silicon-Oil Enhancing O2 Transport in a Porous Electrode. *Electrochim. Acta* **2011**, *56* (13), 4797–4802.

(31) Neumann, B.; Vincent, B.; Krustev, R.; Mü, H.-J. Stability of Various Silicone Oil/Water Emulsion Films as a Function of Surfactant and Salt Concentration. *Am. Chem. Soc.* **2004**, *20* (11), 4336–4344.

(32) Sainath, K.; Ghosh, P. Stabilization of Silicone Oil-in-Water Emulsions by Ionic Surfactant and Electrolytes: The Role of Adsorption and Electric Charge at the Interface. *Ind. Eng. Chem. Res.* **2013**, *52* (45), 15808–15816.

(33) Nazir, H.; Zhang, W.; Liu, Y.; Chen, X.; Wang, L.; Naseer, M. M.; Ma, G. Silicone Oil Emulsions: Strategies to Improve Their Stability and Applications in Hair Care Products. *Int. J. Cosmet. Sci.* **2014**, *36* (2), 124–133.

(34) Mehta, S. C.; Somasundaran, P. Mechanism of Stabilization of Silicone Oil-Water Emulsions Using Hybrid Siloxane Polymers. *Am. Chem. Soc.* **2008**, *24* (9), 4558–4563.

(35) Mehta, S. C.; Somasundaran, P.; Kulkarni, R. Variation in Emulsion Stabilization Behavior of Hybrid Silicone Polymers with Change in Molecular Structure: Phase Diagram Study. *J. Colloid Interface Sci.* **2009**, *333*, 635–640.

(36) Jalani, G.; Jeyachandran, D.; Bertram Church, R.; Cerruti, M. Graphene Oxide-Stabilized Perfluorocarbon Emulsions for Controlled Oxygen Delivery. *Nanoscale* **2017**, *9* (29), 10161–10166.

(37) Wu, Y.; Zhang, F.; Wang, T.; Huang, P.-W.; Filippas, A.; Yang, H.; Huang, Y.; Wang, C.; Liu, H.; Xie, X.; Lively, R. P.; Liu, N. A Submillimeter Bundled Microtubular Flow Battery Cell with Ultrahigh Volumetric Power Density. *Proc. Natl. Acad. Sci.* **2023**, *120* (2), e2213528120.